Characterization of deformational isomerization potential and interconversion dynamics with ultrafast x-ray solution scattering

Natalia E. Powers-Riggs,[†,⊥] Benedikt O. Birgisson,[‡] Sumana L. Raj,[†,#] Elisa Biasin,[†,@] Philipp Lenzen,[¶,△] Diana Bregenholt Zederkof,[¶,▽] Morten Haubro,[¶] Dagrún K. V. Tveiten,[‡] Robert W Hartsock,[†] Tim B. van Driel,[§] Kristjan Kunnus,[§] Matthieu Chollet,[§] Joseph S. Robinson,[§] Silke Nelson,[§] Ruaridh Forbes,[§] Kristoffer Haldrup,[¶] Kasper Steen Pedersen,[‖] Gianluca Levi,[‡] Asmus Ougaard Dohn,[¶,††] Hannes Jónsson,[‡] Klaus Braagaard Møller,[‖] Adi Natan,[*,†] Martin Meedom Nielsen,[*,¶] and Kelly Gaffney[*,†]

†*PULSE Institute, SLAC Accelerator National Laboratory, Stanford University, Stanford, California, USA*

‡*Science Institute and Faculty of Physical Sciences, VR-III, University of Iceland, 107 Reykjavík, Iceland*

¶*Department of Physics, Technical University of Denmark, 2800 Lyngby, Denmark*

§*LCLS, SLAC National Laboratory, Menlo Park, California, USA*

‖*Department of Chemistry, Technical University of Denmark, 2800 Lyngby, Denmark*

⊥*Current Affiliation: Chemistry Department, University of San Francisco, San Francisco, California, USA*

#*Current Affiliation: LCLS, SLAC National Laboratory, Menlo Park, California, USA*

@*Current Affiliation: Physical Sciences Division, Physical and Computational Sciences Directorate, Pacific Northwest National Laboratory, Richland, WA, USA*

△*Current Affiliation: PULSE Institute, SLAC Accelerator National Laboratory, Stanford University, Stanford, California, USA*

▽*Current affiliation: Scientific Instrument Femtosecond X-ray Experiments, European XFEL GmbH*

Abstract

Dimeric complexes composed of d^8 square planar metal centers and rigid bridging ligands provide model systems to understand the interplay between attractive dispersion forces and steric strain, in order to assist the development reliable methods to model metal dimer complexes more broadly. $[Ir_2(dimen)_4]^{2+}$ (dimen = paradiisocyanomenthane) presents a unique case study for such phenomena, as distortions of the optimal structure of a ligand with limited conformational flexibility counteracts the attractive dispersive forces from the metal and ligand to yield a complex with two ground state deformational isomers. Here, we use ultrafast X-ray solution scattering (XSS) and optical transient absorption spectroscopy (OTAS) to reveal the nature of the equilibrium distribution and the exchange rate between the deformational isomers. The two ground state isomers have spectrally distinct electronic excitations that enable the selective excitation of one isomer or the other using a femtosecond duration pulse of visible light. We then track the dynamics of the non-equilibrium depletion of the electronic ground state population – often termed the ground state hole – with ultrafast XSS and OTAS, revealing a restoration of the ground state equilibrium in 2.3 ps. This combined experimental and theoretical study provides a critical test of various density functional approximations in the description of bridged d^8-d^8 metal complexes. The results show that density functional theory calculations can reproduce the primary experimental observations if dispersion interactions are added and a hybrid functional, which includes exact exchange, is used.

Introduction

The close interplay between metal–metal distance and optical and reactive properties[1] of d^8–d^8 metal complexes yield a configurable class of molecules with potential applications in sensing, light-emitting devices,[2] and catalysis.[3] According to the molecular orbital configuration shown schematically in Fig. 1, these square planar d^8 sub-units are metal–metal non-bonding: the HOMO d_{z^2} orbitals in the monomer are doubly occupied, leading to fully

occupied $d_{z^2}\sigma$ and $d_{z^2}\sigma^*$ orbitals in a dimeric complex.[1] Nonetheless, many d^8 monomers self-assemble into oligomers[4,5] and polymers, raising the question of what controls the monomer–monomer interactions. For oligomers with aromatic ligands, quantum chemical calculations indicate the polarizability of the ligands can be critical to the chemical driving force for dimer formation.[6] However, the formation of oligomers in complexes with non-aromatic ligands[4] demonstrates the importance of additional non-covalent bonding interactions, such as the dispersion forces between the metal atoms, or between the metal atoms and surrounding ligands. This poses a challenge when modelling the structure of such complexes.

Dimeric complexes of the type $[M_2(dimen)_4]^{2+}$ (MDimen, where dimen = para-diisocyanomenthane, and M = Rh or Ir, see Figure 1), present a particularly interesting model to study these nonbonding interactions. Each dimen bridging ligand lacks the polarizability—and by extension, attractive dispersion forces and tendency to aggregate—of an aromatic linker, and the rigid cyclohexane unit of the ligand also presents a steric constrain that limits the conformational flexibility. This constraint, in conjunction to the square planar geometry typical of M–isocyano bonding, leads to a spacing of 4 – 5 Å between metals, compared to the ∼3.3 Å metal–metal distance ($d_{\text{M-M}}$) displayed in complexes with nonrigid alkyl ligands possessing the same number of spacer carbon atoms.[7] Early analysis[8] of the crystal structure of dimeric rhodium and iridium complexes indicate that the type of metal center also has an influence on the equilibrium geometry, since across several isocyanide bridged ligands, the equilibrium Ir-Ir distance (3.6 – 4.4 Å) is consistently shorter than the equilibrium Rh-Rh distance (3.9 – 4.5 Å).[8]

These modifications in metal–metal distance generate significant changes in the UV–visible absorption spectrum. In d^8–d^8 metal complexes, the lowest energy electronic transition results from excitation of the HOMO antibonding $d_{z^2}\sigma^*$ orbital to the LUMO bonding $p_z\sigma$ orbital (see molecular orbital diagram shown in Figure 1d). This transition significantly red-shifts as the metal–metal distance shortens, as antibonding (HOMO) and bonding (LUMO) orbitals become destabilized and stabilized, respectively.[1] This correlation between struc-

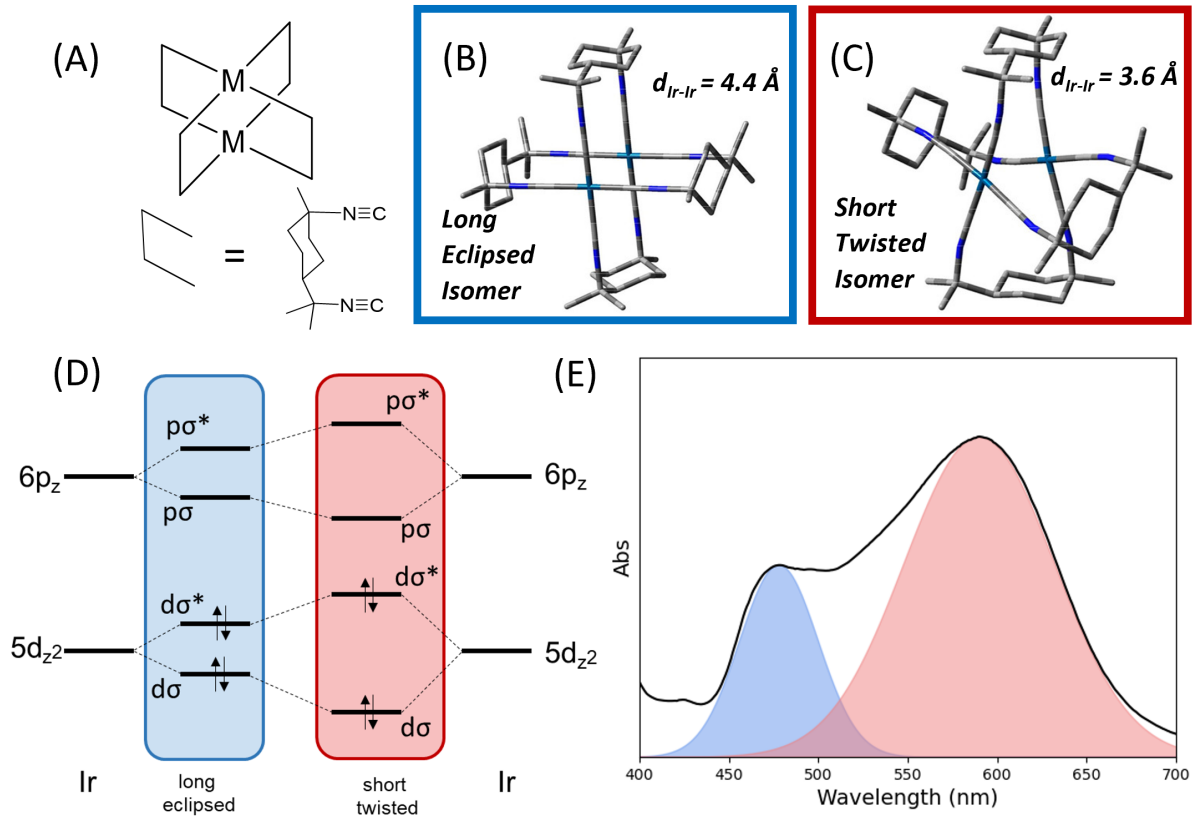

Figure 1: A) Schematic molecular structure of a MDimen complex, with detailed depiction of the dimen ligand. Visualization of the two deformational isomers of IrDimen, the long and eclipsed isomer (B), and the short and twisted isomer (C). D) Molecular orbitals involved in the lowest energy electronic transitions in the IrDimen complex. E) UV-vis absorption spectra of IrDimen, with shaded regions depicting the bands associated with transitions arising from the populations of different isomers.

ture and absorption properties provides a means for gaining preliminary information on the equilibrium structure in solution. Both rhodium and iridium dimen complexes can display a range of M-M distances in the solid state by varying the counter ions, but their distinct solution-phase spectra indicate different equilibrium geometries. In solution, the UV–visible absorption spectrum of RhDimen shows a single broad, asymmetric band centered at 423 nm,[9,10] similar to the absorption spectrum of the RhDimen complex with a 4.5 Å Rh-Rh distance. This single, broad peak corresponding to a structure with a long M-M distance indicates the presence of a broad distribution of conformations around a single equilibrium

isomer in solution, and that the steric hinderence from the dimen ligands dominates over attractive forces such as dispersion interactions. IrDimen exhibits two peaks in the solution phase UV-visible absorption spectrum, at 480 and 585 nm, suggesting the presence of populations of distinct deformational isomers (Figure 1E). Correlation between the crystal structures and the UV-visible spectrum identifies the peak at 480 nm as arising from an isomer with a long Ir–Ir distance and an eclipsed ligand structure, hereafter the "long/eclipsed isomer" (Fig. 1B), while the peak at 585 nm is assigned to a shorter Ir–Ir distance and a twisted ligand structure, or "short/twisted isomer" (Fig. 1C).[8] Variable temperature absorption revealed the two peaks are in equilibrium, and can undergo temperature dependent interconversion, though the lack of an isosbestic point in the temperature dependent spectra indicates thermally populated Franck-Condon active vibrations influence the absorption spectrum.[11]

Understanding the forces at play is key to developing design principles for d^8-d^8 dimer complexes with specific electronic properties. The distinct equilibrium isomers of IrDimen create an opportunity to further understand the interplay between different kinds of intramolecular interactions. Investigating the dynamics of interconversion provides further insight into relative free energy levels and barrier heights between equilibrium isomers. However, determination of the equilibrium structures of the isomers of IrDimen through computational approaches has thus far proved to be challenging.

Previous theoretical studies on IrDimen used density functional theory (DFT) with various density functional approximations[1,10,12,13] and classical harmonic force field approximations for the Ir-Ir interaction potential[11] to determine the balance of forces that dictate the structure and dynamics of IrDimen. These prior DFT studies provide essential context for our computational findings. Calculations with the generalized gradient approximation (GGA) exchange-correlation functional PBE as well as the hybrid functionals PBE0 and B3LYP, which include a fraction of exact exchange, find only one minimum energy geometry, corresponding to a long/eclipsed isomer, and overestimate the Ir-Ir distance by 0.2-0.3

Å. Adding a long-range dispersion interaction correction, such as D3, to the PBE0 functional improves the estimate of the Ir-Ir distance of the long/eclipsed isomer[1,10,12] and leads to a second minimum energy geometry, corresponding to a short/twisted isomer. The improved structure upon inclusion of the dispersion contribution indicates that long-range dispersion effects could be central in shaping the electronic potential energy surface of the ground state of IrDimen.

Dispersion corrections in DFT are typically functional dependent, raising the question of which combination of density functional approximation and dispersion correction can best describe the ground state structure of (molecules like) the IrDimen complex. While several benchmarks of the performance of density functional approximations in terms of their ability to describe complexes containing a single transition metal atom exist,[14–16] fewer benchmarks address d^8-d^8 bimetallic complexes.[6,17] Moreover, previous computational studies on IrDimen did not address the extent to which density functional approximations can describe the potential energy landscape of the complex including the barrier between the two minima.

In the absence of reliable theoretical estimates, an accurate experimental characterization is imperative. Extracting quantitative information about equilibrium populations from the UV–visible spectrum, as discussed prior, proves inconclusive. Specifically, quantitative analysis of the temperature dependent UV–visible spectra is impeded by (1) the different oscillator strengths associated with the two isomers likely due to non-Condon effects and (2) the large Franck-Condon factors for the low frequency Ir–Ir stretching vibration, making the shape of peaks within the absorption spectrum strongly temperature dependent.

Given the complexity of interpreting IrDimen isomer populations through optical spectroscopy, we have found time-resolved X-ray solution scattering (XSS) to be a particularly effective probe to study the IrDimen isomerization, as it directly measures nuclear geometry, and is thus unaffected by changes in oscillator strengths. Time-resolved XSS, with an optical pump pulse exciting the sample, directly measures optically induced changes in the structure of the complex, and can be used to map the electronic ground state potential

energy surface.[18,19] Time-resolved XSS has been successfully used to elucidate the photoinduced structural dynamics of IrDimen.[20,21] However, due to experimental limitations, previous time-resolved XSS studies were unable to draw clear conclusions regarding the rate of interconversion between the IrDimen ground state isomers.

Haldrup and coworkers report that the IrDimen XSS signal acquired 100 ps after photoexcitation could be best fit when the model included two equilibrium ground state structures with Ir–Ir distances of 3.6 Å and 4.3 Å, consistent with crystal structure analysis.[21] In this study, the high energy X-ray probe at the European Synchrotron Radiation Facility (ESRF) provided the necessary spatial resolution to confidently determine the ground state structure, but the limited time resolution did not enable the investigation of ground state isomerization dynamics. van Driel and coworkers[20] later performed time-resolved XSS measurements of IrDimen at the Linac Coherent Light Source (LCLS) with sub-picosecond time resolution, but with longer wavelength X-ray pulses. Through these experiments, van Driel and coworkers were able to identify excited state population dynamics, specifically a contraction of the Ir-Ir distance within 300 fs, but were unable to isolate in the scattering signal the contributions from ground state isomerization dynamics. This reflects the challenges of differentiating the many contributions to an ultrafast XSS signal with measured momentum transfer of $Q < 4.5$ Å^{-1}.

To address these challenges, we employ here ultrafast XSS at high photon energy and momentum transfer up to 8 Å^{-1}, which makes it possible to accurately track the relative populations of the deformational isomers as they evolve in time. In the presented experiments, we preferentially photoexcite the equilibrium population of the long/eclipsed isomer and observe changes to the overall ground state population with a delayed X-ray probe pulse. This preferential depopulation of the long isomer creates a nonequilibrium distribution on the electronic ground state potential energy surface that re-establishes equilibrium according to a thermal reaction rate dictated by the energy barrier between the two minima on the potential energy surface corresponding to the two isomers. Please find a schematic

of the population dynamics in Figure 2. Figure 2(A) depicts the excitation process. Photoexcitation with a 480 nm pump pulse creates an electronically excited population with a non-equilibrium structural distribution on the excited state potential energy surface, here $^1(d\sigma^* p\sigma)$. It then undergoes structural reorganization to form the excited state equilibrium geometry, depicted with process (1). In a concomitant process, the electronic ground state, having a non-equilibrium distribution of the two structural isomers, undergoes structural reorganization, (A), which we describe below. Figure 2(B) shows the ground state population ($P_{\mathrm{GS}}^{\mathrm{eq}}$) (shaded purple) as a function of the Ir-Ir distance ($d_{\mathrm{Ir\text{-}Ir}}$) when in equilibrium. Figure 2(C) depicts the system immediately upon photoexcitation, where the ground state has been selectively depopulated, forming electronic excited state (P_{ES}) (shaded red) and depleted electronic ground state ($P_{\mathrm{GS}}^{\mathrm{noneq}}$) (shaded blue) populations. The gray dashed line shows the original ground state equilibrium population. Figure 2(D) depicts ground and excited state populations some time after photoexcitation, in the case where only process (1) occurs, or reorganization of the excited state, with no changes to the ground state. The nonequilibrium difference population (P_{ES}+$P_{\mathrm{GS}}^{\mathrm{noneq}}$-$P_{\mathrm{GS}}^{\mathrm{eq}}$) where the electronic excited state has nearly reached its equilibrium, but the ground state distribution of the deformational isomers has not changed, is also shown. Following geometry equilibration on the singlet excited state potential, the molecule undergoes intersystem crossing to the structurally similar ^{3}dσ^*pσ state with a 72 ps time constant and decays to the ground state with a 300 ns lifetime.[10,21] Lastly, Figure 2(E) shows the population distribution for a system where both the (1) and (A) processes have occurred, and both electronic excited state and ground state hole populations have reached their structural equilibrium.

This approach of selectively exciting a narrow spectral range of a broad inhomogeneous band is a technique known as hole burning and has been shown to be a powerful tool to elucidate nonequilibrium dynamics in the ground state.[22] While hole burning dynamics have largely been probed with optical spectroscopy,[23] they can also be probed with time-resolved XSS to characterize the ground state potential energy surface, as recently demonstrated for

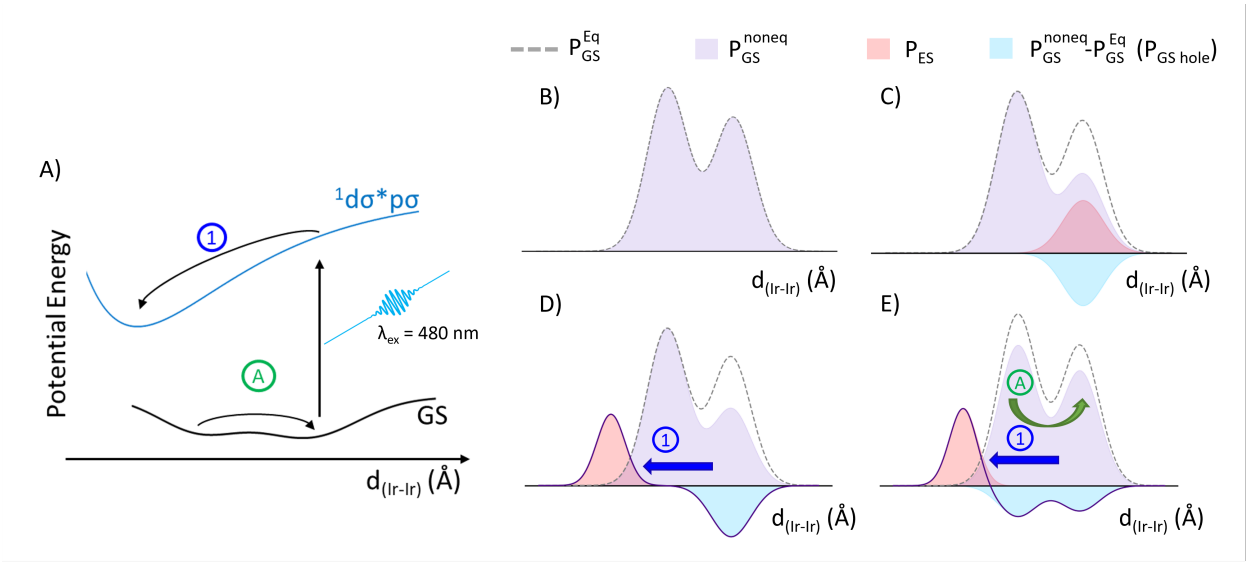

Figure 2: Schematic depictions of the hole burning process and following nonequilibrium dynamics. A) Ground state and excited state potential energy surfaces of IrDimen. Following excitation, the excited state nonequilibrium population of structures undergoes relaxation to the energetic minimum of the respective potential energy surface (process (1)). The ground state concurrently undergoes process (A), where the equilibrium between the population of the two isomers is reestablished. The population dynamics are represented in B)-E), as a function of Ir-Ir distance. The ground state population at equilibrium is represented by the gray dashed line, the nonequilibrium ground state population ($P_{\mathrm{GS}}^{\mathrm{noneq}}$) is represented by the shaded purple curve. B) IrDimen ground state population at equilibrium. C) The populations immediately upon photoexcitation where the long/eclipsed isomer is selectively excited, creating a nonequilibrium excited state population (P_{ES}) (red) and a ground state hole ($P_{\mathrm{GS}}^{\mathrm{noneq}}$-$P_{\mathrm{GS}}^{\mathrm{eq}}$) (blue) D) depicts cases without ground state reorganization, where only process (1) occurs, shown by the excited state population reaching shorter Ir-Ir distances. E) shows the result of both (A) and (1), where in addition to excited state reorganization, the ground state has restored equilibrium.

the $[Pt_2(pyrophosphite)_4]^{4-}$.[24] In the presented experiment, the high-energy XSS probe is used to robustly determine the equilibrium rate constant for interconversion between the long/eclipsed and short isomers, as well as the equilibrium ratio between the conformations. This enables us to estimate the magnitude of the relative free energy barrier that controls the isomer interconversion and also provides a means for assessing the ability of electronic structure methods to describe the potential energy surface of a metal-metal complex such as IrDimen, which has been a long-standing challenge for theory.[25] We evaluate the performance of a large range of density functional approximations and dispersion corrections against the experimental results and further compute the minimum energy path and energy barrier between the different minimum energy geometries. This test provides insights into the reaction coordinate for interconversion between the long/eclipsed and short/twisted isomer, complementing the experimental observations.

Methods

X-ray Experimental Methods

We conducted X-ray scattering measurements at the XCS endstation at the Linac Coherent Light Source (LCLS) at SLAC National Accelerator Laboratory, under conditions similar to those previously reported.[26] We delivered the 10 mM solution of IrDimen in acetonitrile to the interaction region through a closed-loop pump, generating in a 50 µm cylindrical jet and full sample refresh for each probe event at 120 Hz. The sample reservoir was kept under He atmosphere, and periodic addition of acetonitrile maintained the reservoir volume of 40 ml. The nozzle and catcher for the jet were contained in a He-filled sample chamber with a kapton-covered window allowing the scattered 18 keV (λ = 0.7Å) X-ray photons to exit the chamber. We collect the scattered X-rays on the Epix 10k 2M detector,[27,28] at scattering angles 2θ between 3° and 55° corresponding to a Q-range of 0.7 to 8 Å^{-1}, $Q = (4\pi \sin(2\theta/2))/\lambda$.

The sample was photoexcited with 480 nm vertically polarized laser pulses generated by optical parametric amplification of the 800 nm fundamental of a titanium:sapphire laser, with pulse durations of 50 fs duration at full width half maximum, 4 µJ of energy per pulse, and a spot size of 75× 75 µm. These excitation conditions lead to single photon absorption and avoid non-linear absorption, as shown in Fig. S1 of the supporting information. The X-ray pulses were used to probe the sample after pumping with the optical laser. The time delay, Δt, between the optical laser excitation and the X-ray probe was varied in order to monitor the change in the scattering signal as a function of Δt. Additionally, we measured the shot-to-shot fluctuations in the relative time of arrival between the X-ray and the optical pulses for each pump/probe event using a timing diagnostic that measures the arrival time of the X-ray probe relative to the optical pump by measuring the increased optical absorption in Si_3N_4 resulting from X-ray generated carriers.[27]

We corrected the shot-to-shot fluctuations in X-ray wavelength using the measured shot-to-shot variation in electron beam energy[29] and the shot-to-shot fluctuations in X-ray pulse intensity with the integrated intensity on the detector. We also corrected detector images for the X-ray polarization, the geometry dependence of each pixel's solid angle coverage, and the geometric dependence of the X-ray absorption through the liquid jet.[29] We prepared a difference signal by first scaling data at all Q values by the average intensity between 4.5 and 6 $Å^{-1}$, then subtracting each optical laser-on shot by the average of 25 optical laser-off shots. We generated the Δt dependent difference scattering signal by sorting the ΔS images by the timing tool measured Δt into bins 20 fs wide. Lastly, we fit the two-dimensional Δt dependent images into isotropic and anisotropic Q-dependent difference signals, as described in detail by Biasin *et al.*[30] Our present study focuses on the isotropic difference signal, referred to as $\Delta S(Q, \Delta t)$ throughout the manuscript.

Computational Methods

We performed geometry optimizations of IrDimen using DFT calculations with several different functionals and corrections to include dispersion interactions. The functionals used include GGA, meta-GGA, hybrid and long-range corrected exchange-correlation functionals. The dispersion corrections employed were D4,[31] D3[32] with the Becke-Johnson damping function (BJ),[33–35] as well as D3BJ[36] with three body interactions (D3BJ-ATM).[37] In all calculations, the orbitals were represented with the def2-TZVP basis set.[38] For each combination of functional and dispersion correction, we performed two geometry optimizations: one starting from an initial guess for a long/eclipsed structure and the other starting from the short/twisted isomer structure. We performed all calculations without solvent, unless otherwise stated. To identify the structure of the transition state for interconversion between the two deformational isomers, we performed minimum energy path calculations using the Nudged Elastic Band (NEB)[39,40] method with the climbing image algorithm[41] and energy-weighed spring constants.[42] An extended description of the simulation methods used can be found in the supporting information.

Results and Discussion

Ultrafast X-ray Solution Scattering:

From the two-dimensional detector scattering signal for each shot, the isotropic component of the signal was extracted[30] and displayed with respect to Q and delay time t, as shown in Figure 3a. The positive signal at low Q corresponds to a decrease of atomic-pair distances,[43] which follows with the expected contraction of the Ir–Ir distance upon photoexcitation.[20,43,44] The increasing scattering signal intensity within the first two picoseconds corresponds to the nuclear rearrangement of the system following instantaneous electronic rearrangement. Additionally, we observe oscillatory features within the first 500 femtoseconds, which correspond

to the oscillations of the Ir–Ir contraction, as previously reported.[20]

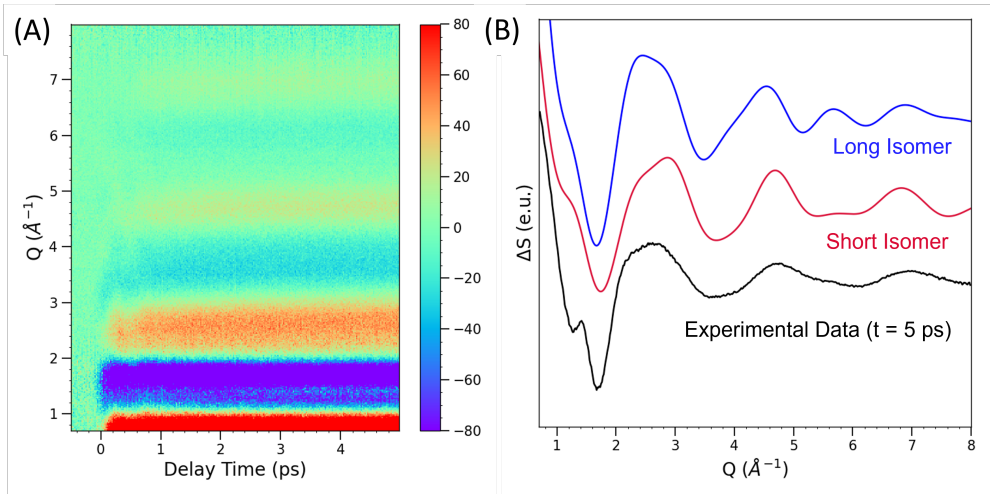

Figure 3: A) Difference X-ray solution scattering for IrDimen in aceotnitrile. B) Experimental ifference XSS signal at delay time 5 ps (black) and simulated curves with an excited state Ir-Ir distance of 2.9 Å, and ground state distances of 4.5 Å (blue) and 3.5 Å (red).

The measured difference scattering signal is a combination of the changes to the solute, solvent, and solute–solvent interactions. Prior studies have demonstrated that solvent and solvent–solute signals are primarily localized at Q <3 Å^{-1},[20] so data at higher Q can be confidently assigned to changes in the solute structure. This assumption is further supported by comparison of IrDimen solutions in dimethyl formamide (DMF) and acetonitrile (MeCN), where any differences between these two measurements due to solvation dynamics occur for Q-values below 3 Å^{-1}. (Figure S2)

The contribution of the solute to the total difference signal can be determined by simulating the scattering signal for representative molecular structures. Simulated isotropic scattering as a function of Q can be calculated by assuming the independent atom model approximation and using the Debye equation,

$$S(Q) = \sum_{i,j}^{N} \left[f_i(Q) f_j(Q) \frac{\sin(Q r_{ij})}{(Q r_{ij})} \right] \quad (1)$$

where i, and j, represent all atoms in the molecule. The first term corresponds to the atomic scattering factor $f_i(Q)$ and $f_j(Q)$for atoms i and j, and r_{ij} is the interatomic distance between

atoms i and j, making the second term correspond to the interference function between all pairs of atoms i and j. Subtracting the scattering curves of a proposed ground state structure from scattering associated with a proposed excited state structure presents a simulation of the solute contribution of the scattering signal, $\Delta S_{\text{Solute}}(Q) = S_{\text{Excited State}}(Q) - S_{\text{Ground State}}(Q)$.

The high time resolution afforded by the short pulses at LCLS, in conjunction with the high spatial resolution of the scattering signal from the high photon energy, presents a new opportunity to observe ground state dynamics of IrDimen immediately following photoexcitation. The value of this experimental set up can be underscored by qualitatively comparing experimental data at 5 picoseconds to simulated difference signals (Figure 3b). The two simulated signals have the same excited state geometry, one is derived from a ground state matching the long/eclipsed isomer geometry and the other from the short/twisted isomer. This comparison reveals several key insights. The difference between the simulated structures is more pronounced at high Q and the experimental data appears to have contributions from multiple ground state structures, consistent with the observations made by Haldrup *et al.*[21] Both these observations underscore the need for larger Q-range. Lastly, despite exciting at a wavelength that would preferentially depopulate the long/eclipsed isomer, the experimental data shows better agreement with the simulated signal from the short/twisted isomer, indicating any re-equilibration occurs within five picoseconds, demonstrating the importance of high time resolution.

Distribution Fitting:

To accurately capture the distributed nature of the IrDimen ground state, we use a distribution-based fitting method. By fixing the Ir-Ir pair distance at a set value and performing a geometry optimization on all other atoms, we create a library of IrDimen structures in both the excited and ground states. For each structure, we simulate the scattering signal, resulting in a library of scattering signals for each Ir–Ir distance ranging from 2.5 to 5.0 $\AA$ in increments of 0.05 Å. These scattering patterns, along with the scattering contribution from bulk sol-

vent heating, were weighted by the distribution term w, which we determined by minimizing the residual of the sum of all structures with the experimental data through a convex optimization method.[45] This approach allows for the possibility of a distribution of structures contributing to the final scattering signal, rather than enforcing two specific ground state structures with specific geometries. A detailed discussion of the fitting procedures can be found in the supporting information.

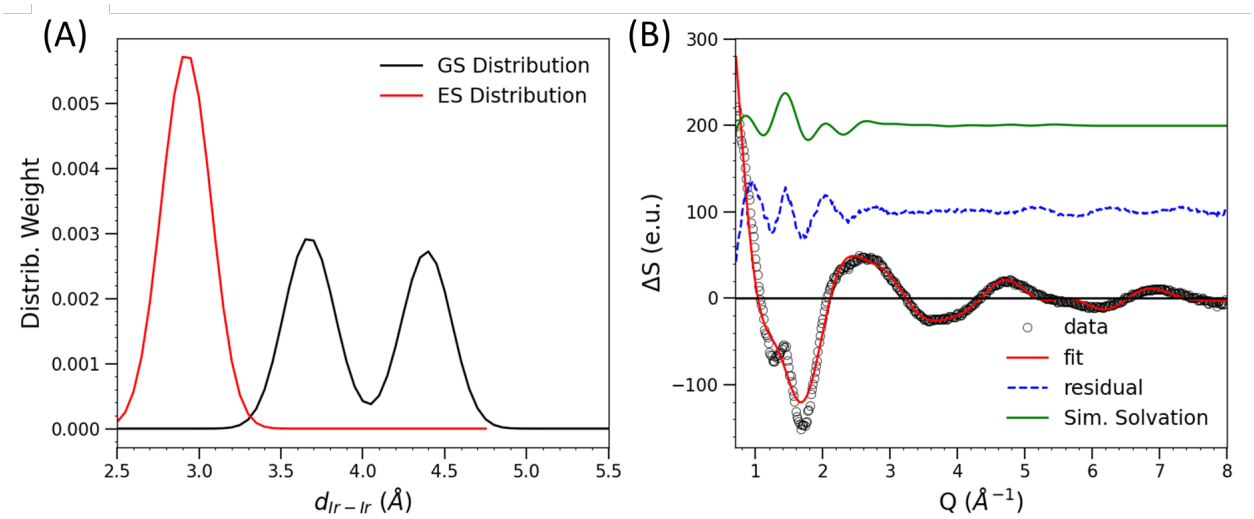

Figure 4: A) Weighting terms w for each Ir-Ir distance for fit of data at 5 ps. B) Overlaid data (black), fit (red) and resulting residual (blue) for averaged 4.5-5 ps time delay. Simulated scattering signal due to changes in solvation as calculated previously[20] is shown in green.

The resultant fit shows good agreement with the data at 5 ps for $Q > 3$ Å^{-1} (Figure 4). The most significant deviation from the predicted structure occurs at low-Q. This low-Q residual shows strong similarity to the calculated signal from solute–solvent interactions, as outlined in previous work.[20] The fit describes a distribution of ground state Ir-Ir bond lengths with an excited state narrowly localized around one M–M distance. Critically, the ground state requires two distinct M–M distances to effectively fit the experimental findings. It is notable that a majority of the ground state contribution comes from the short and twisted conformation, demonstrating the electronic ground state bond isomerization is largely complete within the 5 ps measurement window.[21]

This time-resolved fit was obtained by independently fitting the XSS at each delay time

using the distribution method described above (Figure 5). Note that the early time dynamics (t < 1.5 ps) are not well captured by this fitting method. This discrepancy reflects the emphasis on sparse, non-overlapping Ir-Ir bond distributions for the ground and excited state. This suppresses population dynamics where the ground and excited state distributions overlap, a property that dominates for short time delays. This artifact of our analysis method does not affect the results from time delays beyond 1.5 ps. We draw this conclusion from the fact that the total excited state population reaches a steady state value for time delays beyond 1.5 ps, as shown in Fig. 5C.

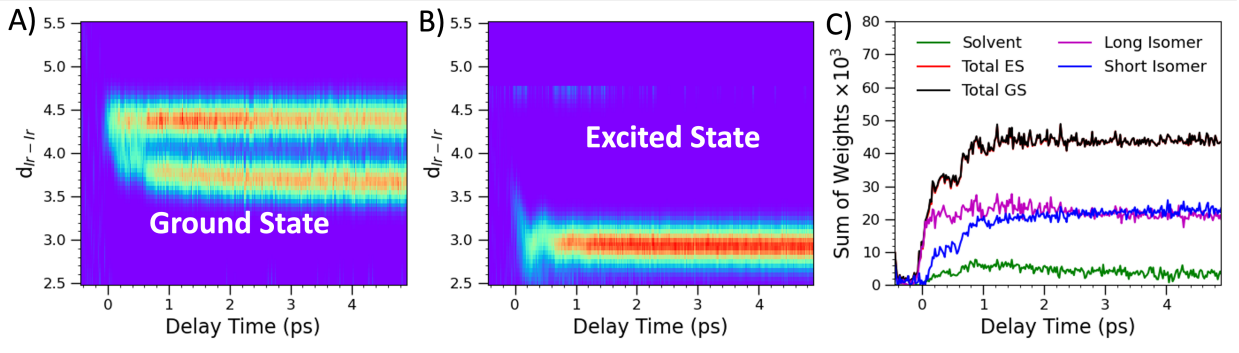

Figure 5: 2D contour map of weighting, at each time delay and Ir-Ir distance for the ground state (a) and the excited state (b). Note that the fluctuations at 4.5 Å can be attributed to failures for the fit to capture the data in a reasonable manner at early times. c) Sums of all weighting values at each delay time.

This representation of Ir-Ir distances with respect to time highlights key findings. As depicted in 5B, the excited state population converges onto a single structure with an Ir-Ir distance of 2.9 Å, consistent with prior analysis.[20,21]

The ground state hole dynamics are comparatively more complicated. As depicted in Figure 5C, at time delays less than 1.5 ps, the majority of the ground state scattering is due to depletion of the long/eclipsed GS conformation, following the preferential excitation of the long/eclipsed conformation at 480 nm. However, by a time delay of 5 ps, the ratio of the ground state populations reverses, with the majority of the ground state coming from the short and twisted isomer. This provides clear, qualitative evidence that the ground state bond isomerization occurs on the few picosecond timescale.

Employing a hole-burning technique of selectively depleting one isomer from the ground state allows for indirect probing of of the ground state potential surface. The fast time resolution afforded by LCLS provides the ability to not only extract the final equilibrium constants, but also the rate at which re-equilibration occurs.

The relative population of the long and short isomers can be calculated by summing the weighting values across distances above and below 4.0 Å, respectively. For a delay time of 5 ps, the ratio of short:long isomers is 53:47, with a margin of error of 1.4. This value is in good agreement with the ratio of 55:45 $\pm$ 3.8, extracted from data collected at considerably longer delay times of 100 ps, which is also in line with prior reports,[21] confirming that equilibrium has largely been restored within the 5 picosecond experiment window.

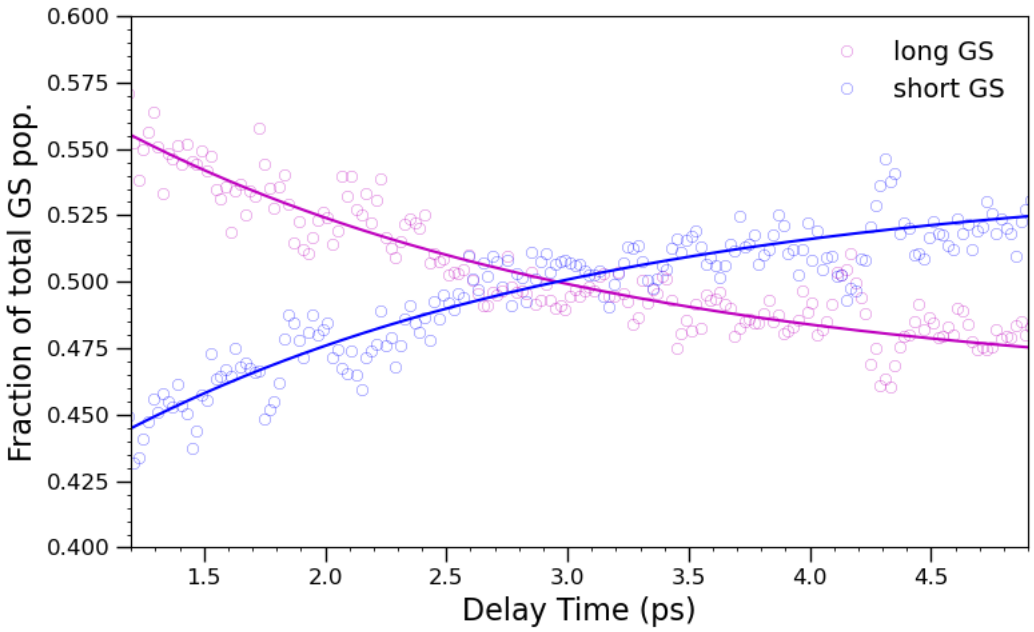

Figure 6: Fraction of the hole population in the long and short ground state isomers as a function of delay time. Weight of long (purple) and short (blue) ground states calculated from distribution fitting shown with open circles, the resulting monoexponential fit depicted with a solid line.

Plotting the relative populations as a percentage of total ground state population with respect to delay time provides a straightforward approach to understanding the kinetic behavior of the system, as seen in Figure 6. We can fit both curves with an $A \rightarrow B$ model,

where A represents the nonequilibrium population after excitation, and B represents the molecules at equilibrium. Fixing the value of B at 55 and 45 for the short and long isomers respectively, based on the 100 ps delay time value, the re-equilibration fits well to a mono-exponential time constant of 2.3 ps. The corresponding fits are depicted with a solid line in Figure 6, against the open circles from the distrubtion fit. This process was also observed in an optical transient absorption spectroscopy (OTAS) experiment, where following excitation at 480 nm, an interconversion of the ground state bleach signal appeared, which could be fit to a similar lifetime of 2.9 ps. See supporting information for a complete discussion of the OTAS data.

Using this observed overall rate, we can estimate relative rates for the forward and reverse deformational isomerization process, as well as estimate the relative barrier heights along the isomerization coordinate. Treating the forward reaction as conversion from the long ground state to the short and twisted conformation, and the backward reaction as the reverse, we see that at equilibrium, the reaction rates should meet the following equality, $k_{L\rightarrow S}n_{long} = k_{S\rightarrow L}n_{short}$. Given the extracted overall rate constant is a sum of the forward and backward rates, and the equilibrium ratio of 55:45 short:long isomer, forward and back rates can be calculated and summarized in Table 1.

Table 1: Rates of interconversion from experimental methods, and the calculated difference in the energy of the short and long isomers: $\Delta E_{S-L} = E_{a,S\rightarrow L} - E_{a,L\rightarrow S}$, where $E_{a,S\rightarrow L}$ and $E_{a,L\rightarrow S}$ are the activation energy of the two isomerization pathways.

Method	$1/k_{total}$ (ps)	$1/k_{L\rightarrow S}$ (ps)	$1/k_{S\rightarrow L}$ (ps)	ΔE_{S-L} (meV)
Scattering	2.3	5.1	4.2	4.99
OTAS	2.9	6.4	5.3	4.84

The difference in activation energy of the isomerization pathways (ΔE_{S-L}), corresponding to the energy difference between the two isomers, can be approximated using Arrhenius equation in the assumption that the pre-exponential factor A for the forward and backward

reactions is the same:

$$\ln k_{L\to S} = \ln A - \frac{E_{a,L\to S}}{k_{\mathrm{b}}T}$$
$$\ln k_{S\to L} = \ln A - \frac{E_{a,S\to L}}{k_{\mathrm{b}}T}$$
$$\ln\left(\frac{k_{L\to S}}{k_{S\to L}}\right) = \frac{E_{a,S\to L} - E_{a,L\to S}}{k_{\mathrm{b}}T} = \frac{\Delta E_{S-L}}{k_{\mathrm{b}}T} \quad (2)$$

where $E_{a,S\to L}$ and $E_{a,L\to S}$ are the activation energy of the isomerization pathways. The value of ΔE_{S-L} obtained in this way is shown in Table 1. The small activation energies and resultant ultrafast rate of isomerization stresses the useful limits of transition state theory which relies on the rate of intra-well isomer equilibration to exceed the rate of inter-well isomer interconversion, but does not invalidate the determination that a small free energy barrier separates the two deformational isomers of IrDimen.[46,47] The qualitative similarity between the measured rates for the deformational isomerization using two fundamentally distinct probes of the isomerization provides confidence we have a robust experimental framework for assessing the molecular properties that control this chemical transformation.

Computational modelling

With the experimental determination of the ground state Ir-Ir distances and population ratios, we have now acquired the necessary benchmarks to critically test how well a range of often used density functionals and long-range dispersion corrections reproduce the experimental findings.

Geometry optimizations

Figure 7 shows the Ir-Ir distances for geometry optimized structures of IrDimen using different combinations of exchange-correlation functionals and dispersion corrections as compared with the experimental values for the Ir-Ir distances of the two deformational isomers. Only the results of calculations that were able to converge on two distinct deformational isomers

with Ir-Ir distances differing by more than 0.2 Å are included in this figure. The results for all the DFT approaches used are depicted in Fig. 10 in the supporting information. We draw three primary conclusions from the comparison of different density functional based calculations to the experimentally extracted structures.

Firstly, we observe the importance of dispersion interactions in correctly simulating isomer structures. Without a dispersion correction, all pure functionals only find a stable long/eclipsed isomer, regardless of the initial guess geometry in the structural relaxation (see Fig. 10 in the supporting information). Moreover, the Ir-Ir distance of this isomer is overestimated on average by ∼0.2 Å compared to experiment, when no dispersion correction is applied to the pure functionals. This is the case for all functionals, apart from r^{2}SCAN, which underestimates it by ∼0.3 Å.

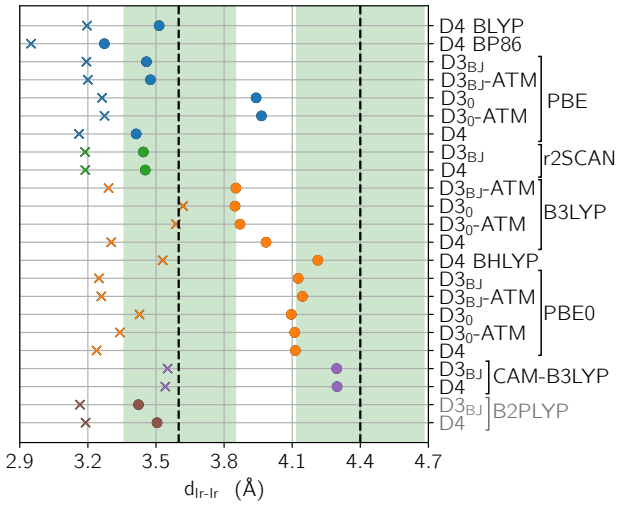

Figure 7: Ir-Ir distances, $d_{\mathrm{Ir-Ir}}$, of the optimized geometries of IrDimen obtained by energy minimization in vacuum using DFT with dispersion corrections, starting from guess structures for the long/eclipsed (•) and short/twisted (×) isomers. The marker colors denote the type of exchange-correlation functional used in the calculation; GGA:blue, Meta-GGA:Green, Hybrid:Orange, Range-Separated:Purple, Double-Hybrid:Brown. The black dashed lines represent the experimentally determined short/twisted and long/eclipsed isomer Ir-Ir distances. The green patches span the experimental uncertainties. The grey labels indicate that no frequency calculations have been performed. Good agreement with the experimental results is obtained only if the calculations use a hybrid functional, which includes exact exchange, together with a dispersion correction.

Secondly, the choice of functional significantly influences the optimal geometries for the

two isomers. For instance, including dispersion corrections in the calculations with GGA and meta-GGA functionals generates local minimum energy eclipsed and twisted isomers, but the calculated Ir-Ir distances underestimate the experimentally observed distances on average by ∼1.0 and ∼0.4 Å for the of the long/eclipsed and short/twisted isomers. Much better results are obtained when hybrid functionals are used together with a dispersion correction, with long/eclipsed- and short/twisted-isomer structures that underestimate the experimental Ir-Ir distance by ∼0.5 Å (∼10 %), on average . The best results are obtained when using the BHLYP, PBE0 and CAM-B3LYP functionals with D4 or D3BJ corrections. Overall, these results indicate that only a hybrid functional, which includes a fraction of exact exchange, and dispersion corrections can correctly describe the balance between attractive interactions and ligand strain in the IrDimen complex leading to an accurate structural prediction. The importance of dispersion interactions is in line with previous studies on molecules containing only a single metal atom.[48]

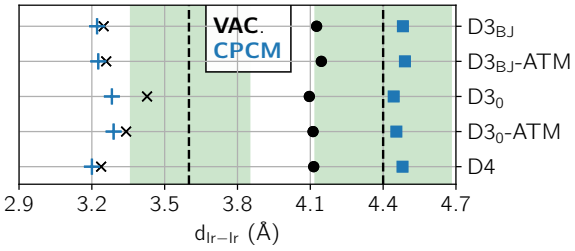

Figure 8: Ir-Ir distances, $d_{\mathrm{Ir-Ir}}$, of the optimized geometries of IrDimen obtained by minimizing the energy given by the hybrid functional PBE0 with dispersion corrections in vacuum (black markers) and in acetonitrile as modeled with a polarizable continuum model (CPCM, blue markers), starting from guess structures for the long/eclipsed (• and ■) and short/twisted (× and +) isomers. The black dashed lines and green patches indicate the values deduced from X-ray solution scattering measurements and experimental uncertainties, respectively. Including solvent effects in the calculations improves the estimate of Ir-Ir distance for the long/eclipsed isomers.

Thirdly, the inclusion of solute-solvent interactions with a polarizable continuum solvent model (PCSM) improves the accuracy of the calculated isomer structures when compared to experiment (see Fig. 8). For PBE0, the already reasonable match with the experimental values is improved using a PCSM for acetonitrile. Inclusion of solvent effects leads to an

increase in the Ir-Ir distance of the long/eclipsed isomers, giving an error of less than ∼0.1 Å (less than ∼3 %) with respect to the experimental value for this isomer. However, it does not lead to significant changes in the the Ir-Ir distance of the short/twisted isomer. This indicates that solvent screening of the Ir-Ir interactions plays a larger role for the long isomer, where the Ir atoms are more exposed to the solvent.

Energy difference and minimum energy path

For most of the combinations of exchange-correlation functional and dispersion correction that correctly identified two distinct isomers, the energy of the long/eclipsed isomer is higher than that of the short/twisted isomer (see Figure 12 in the supporting information) with the short/twisted isomer having an average energy 39 meV lower than the long/eclipsed isomer. Inclusion of the entropy difference (obtained via the frequency calculations) in the Gibbs free energy at 298 K between the two isomers makes the long/eclipsed isomer more stable by 26 meV because this isomer has lower frequency vibrational modes with correspondingly higher entropy. For the PBE0 hybrid functional with dispersion corrections, which displayed one of the best structural agreements with the experiments among all approaches, the Gibbs free energy of the long/eclipsed isomer is lower than that of the short/twisted isomer by ∼50 meV. The small free energy difference between the two isomers (the value of $k_b T$ at room temperature is ∼25 meV) and the greater stability of the short/twisted isomer at low temperature are qualitatively consistent with the XSS measurement and previous temperature-dependent optical absorption measurements,[11] which reveal a preference for the short/twisted isomer at lower temperature. However, we note that for some of the investigated approaches, intermediate energy minima could be found, indicating a rather shallow and rugged potential energy surface, which precludes a direct comparison with the experimentally determined population ratio. Fig. 9 shows the minimum energy path between the two deformational isomers obtained with the PBE0 hybrid functional, D4 dispersion correction and CPCM solvation. The images are started out evenly spaced along $\Delta\mathbf{R}_n = \Sigma_i^n \sqrt{\Sigma_j^{3N} \left(q_j^i - q_j^{i-1}\right)^2}$,

but during the run, the energy-weighted spring algorithm causes images at the highest energies to experience stronger spring constants and images at the end points to experience lower spring constants. This leads to the congregation of images at the barrier top, which increases our information in vicinity of the saddle point, giving a better estimate of the tangents around it. This calculation confirms that the potential energy surface is shallow with a very small energy barrier of ∼15 meV. The strong anharmonicity of the potential energy surface does not enable the use of harmonic transition state theory to estimate the rate of interconversion between the two isomers, however the presence of a very small barrier is in agreement with the experimental observation that the interconversion is ultrafast with a time scale between 2-3 ps. Figure 9 shows the change in Ir-Ir distance and angle between square planar units along the minimum energy path confirming the dominant role of Ir-Ir contraction and torsion around the Ir-Ir bond in the interconversion between deformational isomers of IrDimen. as proposed by Hill, Gray, and Hunter.[11,44] An interesting distinction, however, is the structure of the transition state. As shown in Fig. 9, the transition state has a nearly eclipsed structure, while the empirical force-field developed by Hunter shows significant twisting about the Ir-Ir bond at the transition state.[11]

Closing Remarks

The d^8-d^8 metal dimer systems have absorption and emission properties that are highly sensitive to metal-metal distances. IrDimen provides a particularly interesting model to study these metal-metal interactions experimentally and theoretically because the complex has two distinct electronic ground state structures in equilibrium at room temperature, one with a 3.6 Å and the other with a 4.4 Å Ir-Ir bond length. The steric force of the cyclohexane in the dimen ligand pushes the two square-planar components of the dimer away from one another, while an attractive dispersion force from both ligands and metals pulls the moieties closer. The interplay of these counteracting forces results in two isomer conformations in

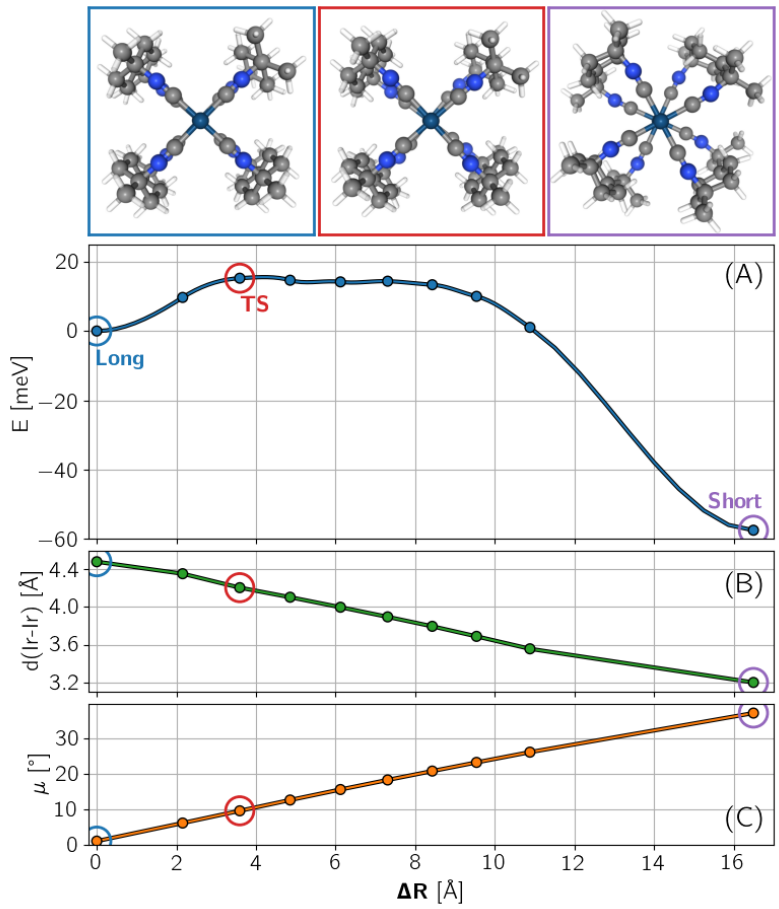

Figure 9: (A) Minimum energy path between the long/eclipsed and short/twisted isomers of IrDimen obtained with the PBE0 functional, D4 dispersion correction, and a continuum solvation model for acetonitrile. The reaction coordinate is given as a cumulative root-mean-square displacement of the positions of the atoms with respect to the long/eclipsed isomer, $\Delta\mathbf{R}_n = \Sigma_i^n \sqrt{\Sigma_j^{3N} \left(q_j^i - q_j^{i-1}\right)^2}$ for images n, where N is the total number of atoms in the complex and q_j are the atomic Cartesian coordinates. The solid line is a piecewise cubic interpolation between the energy of images along the path using the tangential atomic force. (B) Decrease in Ir-Ir distance along the minimum energy path. (C) Increase in the dihedral angle between square planar units of IrDimen (see Fig. 9 in the supporting information for a definition of this angle) along the minimum energy path.

solution. Through ultrafast X-ray solution scattering (XSS) and optical transient absorption spectroscopy (OTAS), we have revealed that the isomers lie in an equilibrium with just over half in the short and twisted conformation. Additionally, we have demonstrated that these two deformational isomers interconvert with an ultrafast time of 2.3 ps.

The experimental results have been used to robustly assess the performance of a large range of density functional approximations, including dispersion interactions, in terms of their ability to describe the potential energy surface of IrDimen. We have determined that hybrid functionals, in conjunction with dispersion corrections and a solvent continuum model, are able to predict two minimum energy geometries in good agreement with the experimental data. The calculated energy differences between isomers– with and without entropy contributions– lie within the expected accuracy of the methods used,[49,50] and match the small differences in energy and activation barrier extracted from experimental methods. This represents a strong development in identifying computational methods to model the multiple conformations of IrDimen.

To further explore the validity of specific computational methods, a broad library of d^8 dimer structures should be examined, both experimentally and computationally. The shallow potential energy surface prevents harmonic approximations, so simulating structures with flexible isocyano- bridging ligands may provide a simple point of comparison. Additionally, a more in-depth comparison with Rh analogue complexes, particularly RhDimen, is vital to gaining deeper insight into the role the metal plays in final structure, as RhDimen is reported to possess a similarly shallow and rugged ground state potential energy surface, with multiple simulated conformations, but experimental evidence suggests the solution phase equilibrium strongly favors the long bond conformation.

Acknowledgement

N.P.R., E.B., S.L.R., A.N., R.W.H., K.J.G. thank U.S. Department of Energy, Office of Science, Office of Basic Energy Sciences, Chemical Sciences, Geosciences and Biosciences Division for supporting this work. B.O.B., G.L. and A.O.D. thank the Icelandic Research Fund (grant agreements no. 207014, 217734 and 196279, respectively). K.H. , D.B.Z and M.H. gratefully acknowledge support from the Novo Nordisk Foundation "NERD" program

under Grant No. NNF20OC0061740. P.L., A.O.D., K.B.M., and M.M.N. gratefully acknowledge the support from the Independent Research Fund Denmark under Grant No. DFF-FP2 8021-00347B. The authors gratefully acknowledge support from the Linac Coherent Light Source, SLAC National Accelerator Laboratory, which is supported by the US Department of Energy, Office of Science, Office of Basic Energy Sciences, under contract no. DE-AC02-76SF00515. The European Synchrotron Radiation Facility (ESRF) is kindly acknowledged for provision of beamtime at the ID09 beamline. The calculations were carried out at the Icelandic High Performance Computing Center (IHPC). The authors thank Elvar Ö. Jónsson for help with the calculations.

References

(1) Gray, H. B.; Záliš, S.; Vlček, A. Electronic structures and photophysics of d8-d8 complexes. *Coordination Chemistry Reviews* **2017**, *345*, 297–317.

(2) Yam, V. W.-W.; Au, V. K.-M.; Leung, S. Y.-L. Light-Emitting Self-Assembled Materials Based on d8 and d10 Transition Metal Complexes. *Chemical Reviews* **2015**, *115*, 7589–7728.

(3) Smith, D. C.; Gray, H. B. Photochemistry of binuclear d8 complexes. *Coordination Chemistry Reviews* **1990**, *100*, 169–181.

(4) Atoji, M.; Richardson, J. W.; Rundle, R. E. On the Crystal Structures of the Magnus Salts, Pt(NH3)4PtCl41. *Journal of the American Chemical Society* **1957**, *79*, 3017–3020.

(5) Chen, Y.; Li, K.; Lloyd, H. O.; Lu, W.; Chui, S. S.-Y.; Che, C.-M. Tetrakis(arylisocyanide) Rhodium(I) Salts in Water: NIR Luminescent and Conductive Supramolecular Polymeric Nanowires with Hierarchical Organization. *Angewandte Chemie* **2010**, *122*, 10164–10167.

(6) Grimme, S.; Djukic, J.-P. Cation-Cation "Attraction": When London Dispersion Attraction Wins over Coulomb Repulsion. *Inorganic Chemistry* **2011**, *50*, 2619–2628.

(7) Smith, D. C. Electronic Structure and Photochemical Reactivity of Binuclear Metal Complexes. PhD Dissertation, California Institute of Technology, Pasadena, California, 1989.

(8) Exstrom, C. L.; Britton, D.; Mann, K. R.; Hill, M. G.; Miskowski, V. M.; Schaefer, W. P.; Gray, H. B.; Lamanna, W. M. Structures of [M2(dimen)4](Y)2 (M = Rh, Ir; dimen = 1,8-Diisocyanomenthane; Y = PF6, Tetrakis[3,5-bis(trifluoromethyl)phenyl]borate, B(C6H5)4) Crystals Featuring an Exceptionally

Wide Range of Metal-Metal Distances and Dihedral Twist Angles. *Inorganic Chemistry* **1996**, *35*, 549–550.

(9) Gerlits, O.; Kovalevsky, A. Y.; Coppens, P. Solid-state spectroscopic properties and the geometry of binuclear rhodium(i) diisocyanoalkane complexes. *Dalton Transactions* **2004**, 3955–3962.

(10) Pižl, M.; Hunter, B. M.; Sazanovich, I. V.; Towrie, M.; Gray, H. B.; Záliš, S.; Vlček, A. Excitation-Wavelength-Dependent Photophysics of d^8-d^8 Di-isocyanide Complexes. *Inorganic Chemistry* **2022**, *61*, 2745–2759.

(11) Hunter, B. M.; Villahermosa, R. M.; Exstrom, C. L.; Hill, M. G.; Mann, K. R.; Gray, H. B. M–M Bond-Stretching Energy Landscapes for $M_2(dimen)_4^{2+}$ (M = Rh, Ir; dimen = 1,8-Diisocyanomenthane) Complexes. *Inorganic Chemistry* **2012**, *51*, 6898–6905.

(12) Záliš, S.; Hunter, B. M.; Gray, H. B.; Vlček, A. Electronic Structures of Reduced and Superreduced Ir_2(1,8-diisocyanomenthane)$_4^{n+}$ Complexes. *Inorganic Chemistry* **2017**, *56*, 2874–2883.

(13) Dohn, A. O.; Jónsson, E. Ö.; Kjær, K. S.; van Driel, T. B.; Nielsen, M. M.; Jacobsen, K. W.; Henriksen, N. E.; Møller, K. B. Direct Dynamics Studies of a Binuclear Metal Complex in Solution: The Interplay Between Vibrational Relaxation, Coherence, and Solvent Effects. *The Journal of Physical Chemistry Letters* **2014**, *5*, 2414–2418.

(14) Garino, C.; Salassa, L. The photochemistry of transition metal complexes using density functional theory. *Philosophical Transactions of the Royal Society A: Mathematical, Physical and Engineering Sciences* **2013**, *371*, 20120134.

(15) Hopmann, K. H. How Accurate is DFT for Iridium-Mediated Chemistry? *Organometallics* **2016**, *35*, 3795–3807.

(16) Bursch, M.; Caldeweyher, E.; Hansen, A.; Neugebauer, H.; Ehlert, S.; Grimme, S. Understanding and Quantifying London Dispersion Effects in Organometallic Complexes. *Accounts of Chemical Research* **2018**, *52*, 258–266.

(17) Novozhilova, I. V.; Volkov, A. V.; Coppens, P. Theoretical Analysis of the Triplet Excited State of the $[Pt_2(H_2P_2O_5)_4]^{4-}$ Ion and Comparison with Time-Resolved X-ray and Spectroscopic Results. *Journal of the American Chemical Society* **2003**, *125*, 1079–1087.

(18) Ihee, H. Visualizing Solution-Phase Reaction Dynamics with Time-Resolved X-ray Liquidography. *Accounts of Chemical Research* **2009**, *42*, 356–366.

(19) Haldrup, K.; Christensen, M.; Meedom Nielsen, M. Analysis of time-resolved X-ray scattering data from solution-state systems. *Acta Cryst A* **2010**, *66*, 261–269.

(20) van Driel, T. B. et al. Atomistic characterization of the active-site solvation dynamics of a model photocatalyst. *Nature Communications* **2016**, *7*, 13678.

(21) Haldrup, K.; Harlang, T.; Christensen, M.; Dohn, A.; van Driel, T. B.; Kjær, K. S.; Harrit, N.; Vibenholt, J.; Guerin, L.; Wulff, M.; Nielsen, M. M. Bond Shortening (1.4 Å) in the Singlet and Triplet Excited States of $Ir_2Dimen_4^{2+}$ in Solution Determined by Time-Resolved X-ray Scattering. *Inorganic Chemistry* **2011**, *50*, 9329–9336.

(22) Brito Cruz, C.; Gordon, J.; Becker, P.; Fork, R.; Shank, C. Dynamics of spectral hole burning. *IEEE Journal of Quantum Electronics* **1988**, *24*, 261–269.

(23) Schilling, D.; Mann, C.; Kunkel, P.; Schöppler, F.; Hertel, T. Ultrafast Spectral Exciton Diffusion in Single-Wall Carbon Nanotubes Studied by Time-Resolved Hole Burning. *The Journal of Physical Chemistry C* **2015**, *119*, 24116–24123.

(24) Haldrup, K. et al. Ultrafast X-Ray Scattering Measurements of Coherent Structural

Dynamics on the Ground-State Potential Energy Surface of a Diplatinum Molecule. *Physics Review Letters* **2019**, *122*, 063001.

(25) Schmidbaur, H.; Schier, A. A briefing on aurophilicity. *Chem. Soc. Rev.* **2008**, *37*, 1931–1951.

(26)

(27) Blaj, G. et al. X-ray detectors at the Linac Coherent Light Source. *Journal of Synchrotron Radiation* **2015**, *22*, 577–583.

(28) van Driel, T. B. et al. The ePix10k 2-megapixel hard X-ray detector at LCLS. *Journal of Synchrotron Radiation* **2020**, *27*, 608–615.

(29) van Driel, T. B.; Kjær, K. S.; Biasin, E.; Haldrup, K.; Lemke, H. T.; Nielsen, M. M. Disentangling detector data in XFEL studies of temporally resolved solution state chemistry. *Faraday Discussions* **2015**, *177*, 443–465.

(30) Biasin, E. et al. Anisotropy enhanced X-ray scattering from solvated transition metal complexes. *Journal of Synchrotron Radiation* **2018**, *25*, 306–315.

(31) Caldeweyher, E.; Bannwarth, C.; Grimme, S. Extension of the D3 dispersion coefficient model. *The Journal of Chemical Physics* **2017**, *147*, 034112.

(32) Grimme, S.; Antony, J.; Ehrlich, S.; Krieg, H. A consistent and accurate ab initio parametrization of density functional dispersion correction (DFT-D) for the 94 elements H-Pu. *The Journal of Chemical Physics* **2010**, *132*, 154104.

(33) Becke, A. D.; Johnson, E. R. A density-functional model of the dispersion interaction. *The Journal of Chemical Physics* **2005**, *123*, 154101.

(34) Johnson, E. R.; Becke, A. D. A post-Hartree–Fock model of intermolecular interactions. *The Journal of Chemical Physics* **2005**, *123*, 024101.

(35) Johnson, E. R.; Becke, A. D. A post-Hartree-Fock model of intermolecular interactions: Inclusion of higher-order corrections. *The Journal of Chemical Physics* **2006**, *124*, 174104.

(36) Grimme, S.; Ehrlich, S.; Goerigk, L. Effect of the damping function in dispersion corrected density functional theory. *Journal of Computational Chemistry* **2011**, *32*, 1456–1465.

(37) Grimme, S. Supramolecular Binding Thermodynamics by Dispersion-Corrected Density Functional Theory. *Chemistry – A European Journal* **2012**, *18*, 9955–9964.

(38) Weigend, F.; Ahlrichs, R. Balanced basis sets of split valence, triple zeta valence and quadruple zeta valence quality for H to Rn: Design and assessment of accuracy. *Physical Chemistry Chemical Physics* **2005**, *7*, 3297–3305.

(39) Ásgeirsson, V.; Jónsson, H. Exploring Potential Energy Surfaces with Saddle Point Searches. *Handbook of Materials Modeling* **2018**, 1–26.

(40) Jónsson, H.; Mills, G.; Jacobsen, K. W. In *Classical and Quantum Dynamics in Condensed Phase Simulations*; Berne, B. J. C. U., Ciccotti, G. U. R. L. S., Coker, D. F. B. U., Eds.; World Scientific, 1998; Chapter 16, pp 385–404.

(41) Henkelman, G.; Uberuaga, B. P.; Jónsson, H. A climbing image nudged elastic band method for finding saddle points and minimum energy paths. *The Journal of Chemical Physics* **2000**, *113*, 9901–9904.

(42) Ásgeirsson, V.; Birgisson, B. O.; Bjornsson, R.; Becker, U.; Neese, F.; Riplinger, C.; Jónsson, H. Nudged Elastic Band Method for Molecular Reactions Using Energy-Weighted Springs Combined with Eigenvector Following. *Journal of Chemical Theory and Computation* **2021**, *17*, 4929–4945.

(43) Christensen, M.; Haldrup, K.; Bechgaard, K.; Feidenhans'l, R.; Kong, Q.; Cammarata, M.; Russo, M. L.; Wulff, M.; Harrit, N.; Nielsen, M. M. Time-Resolved X-ray Scattering of an Electronically Excited State in Solution. Structure of the 3A2u State of Tetrakis-μ-pyrophosphitodiplatinate(II). *Journal of the American Chemical Society* **2009**, *131*, 502–508.

(44) Hartsock, R. W.; Zhang, W.; Hill, M. G.; Sabat, B.; Gaffney, K. J. Characterizing the Deformational Isomers of Bimetallic $Ir_2Dimen_4^{2+}$(dimen = 1,8-diisocyano-p-menthane) with Vibrational Wavepacket Dynamics. *The Journal of Physical Chemistry A* **2011**, *115*, 2920–2926.

(45) Diamond, S.; Boyd, S. CVXPY: A Python-Embedded Modeling Language for Convex Optimization. *Journal of Machine Learning Research* **2016**, *17*, 1–5.

(46) Wigner, E. The transition state method. *Trans. Faraday Soc.* **1938**, *34*, 29–41.

(47) Chandler, D. Statistical mechanics of isomerization dynamics in liquids and the transition state approximation. *The Journal of Chemical Physics* **1978**, *68*, 2959–2970.

(48) Chowdhury, S. R.; Nguyen, N.; Vlaisavljevich, B. Importance of Dispersion in the Molecular Geometries of Mn(III) Spin-Crossover Complexes. *The Journal of Physical Chemistry A* **2023**, *127*, 3072–3081.

(49) Bykov, D.; Petrenko, T.; Izsák, R.; Kossmann, S.; Becker, U.; Valeev, E.; Neese, F. Efficient implementation of the analytic second derivatives of Hartree-Fock and hybrid DFT energies: A detailed analysis of different approximations. *Molecular Physics* **2015**, *113*, 1961–1977.

(50) Perdew, J. P.; Schmidt, K. Jacob's ladder of density functional approximations for the exchange-correlation energy. *AIP Conference Proceedings* **2003**, *577*, 1–20.